



# Dynamic Recrystallization Mechanism and Texture Evolution during Interactive Alternating Extruded Magnesium Alloy

Ronghe Gao<sup>1</sup> · Feng Li<sup>1,2,3</sup> · Huaqiu Du<sup>1</sup> · Pengda Huo<sup>1</sup>

Received: 18 October 2022 / Revised: 3 December 2022 / Accepted: 22 December 2022 / Published online: 8 February 2023  
© The Chinese Society for Metals (CSM) and Springer-Verlag GmbH Germany, part of Springer Nature 2023

## Abstract

Alternating extrusion (AFE) is a new way to effectively alter the texture and enhance the mechanical properties of the extruded bars. However, the mechanisms of microstructure evolution and enhancement of hardness are still unknown by different extrusion ratios (ERs) during extrusion. This work systematically investigated the microstructure and hardness of AZ31 alloy with various extrusion ratios of 8.1, 15.6, and 24.8 by electron backscattered diffraction. The most striking result to emerge from the data is that when the ERs were increased from 8.1 to 15.6, the grain size was refined to 7.13  $\mu\text{m}$ . However, when the ER reached 24.8, the average grain size was 11.43  $\mu\text{m}$ . The proportion of recrystallization was only 2.92%, there was a continuous rotation of sub-grains at coarse grain boundaries, and non-basal slip  $\langle a \rangle$  dislocations were activated and enriched near low-angle grain boundaries. At present, the recrystallization has not been completed. The grains of the product are coarsened, and the hardness is reduced. When  $\lambda = 15.6$ , the AFE has a significant grain refinement effect and the highest hardness value.

**Keywords** Alternate extrusion method · AZ31 magnesium alloy · Extrusion ratio · Grain refinement · Hardness

## 1 Introduction

It is well known that Mg and its alloys, as the lightest metallic structural materials available now, have shown significant potential for applications in armament, aircraft, and aerospace [1–5]. So far, the casting process is generally used for the forming of magnesium alloys. But the casting process itself has many problems, such as casting defects, which restrict the wide use of cast components. Recently,

increasing effort has been put into the research and application of wrought Mg alloys with mechanical properties superior to those of cast Mg counterparts [6, 7]. Li et al. [8] had reported that the unique HCP structure of magnesium alloys results in extremely poor formability at room temperature. Because non-basal slip can only be easily turned on at high temperatures. The extrusion process can make the metal in a state of strong triaxial compressive stress and can achieve grain refinement and texture weakening through the metal plastic working to improve the formability. However, Wang et al. [8] reported that the traditional plastic processing method easily makes the magnesium alloy show a strong basal texture, which could limit its development and application [9]. Sagapuram et al. [10] realized the regulation of magnesium alloy sheet texture through shear-based deformation processing. Tilted-basal textures, wherein the basal poles are inclined from the sheet surface normal, are achieved by this processing. Xu et al. [11] developed an asymmetric extrusion (AE) process for producing magnesium alloy sheets. More recrystallized grains emerge along the thickness direction of the sheet under the impact of asymmetric shear stress, which causes the base texture to rotate approximately 12° in the shear direction. The texture intensity was significantly weakened by asymmetric

Available online at <http://link.springer.com/journal/40195>.

✉ Feng Li  
fli@hrbust.edu.cn

✉ Huaqiu Du  
dhq201302@126.com

<sup>1</sup> School of Materials Science and Chemical Engineering, Harbin University of Science and Technology, Harbin 150040, China

<sup>2</sup> Key Laboratory of Advanced Manufacturing and Intelligent Technology, Ministry of Education, Harbin University of Science and Technology, Harbin 150080, China

<sup>3</sup> Heilongjiang Provincial Key Laboratory of Light Metal Materials Modification and Green Forming Technology, Harbin 150040, China

extrusion. Lu et al. [12] developed a new extrusion method that introduces torsional deformation at the same time as forwarding extrusion. The grain size was drastically reduced, and the average grain size of the product was only 1/10 of the original billet (300  $\mu\text{m}$ ). The fracture strain of the magnesium alloy bars increased from 21 to 29%. Li et al. [13] employed a continuous variable cross-section direct extrusion method to prepare high-performance magnesium alloys. Under the direct extrusion of the third-order continuous variable cross-section, compared with traditional extrusion, the texture intensity is significantly reduced.

Li et al. [14] demonstrated that the unique discrete stem design and loading mode of the AFE method can maximize shear stress, AFE is a new extrusion method with great potential and integration of formability. AFE adopts double punch extrusion technology, and the grain size of magnesium alloy has been dramatically refined. Previous studies have shown that AFE could improve the ductility and tensile strength of magnesium alloy products. However, the grain morphology evolution and refinement mechanism of AFE under different deformation conditions are still unclear.

Ayer [15] researched the products obtained by different extrusion parameters. The research shows that as the ER gradually increases, the microstructure was gradually homogenized, the grain size was also refined to a certain extent, and the mechanical properties increase with the ER enhancement. Alaneme et al. [16], on the other hand, studied Mg-Sm-based alloys with ERs of 6.9, 10.4, and 17.6, respectively. The results revealed that as the ER was raised, the recrystallized grain size gradually rose, accompanied by a drop in tensile strength. In the process of studying different extrusion parameters of Mg-Gd-Y-Zn-Zr alloy, Xu et al. [18]

discovered similar laws. In this work, the grain size of AZ31 magnesium alloy based on the AFE process also showed abnormal growth with the increase of ER. In this paper, the relationship between the deformation degree and grain morphology, texture evolution, and hardness were investigated, and the grain refinement mechanism of alternate extrusion of magnesium alloys at a large ER was analyzed.

In this study, the relationship between the degree of deformation and grain morphology, structural evolution, and microstructure properties were investigated, and the grain refinement mechanism of alternate extrusion of magnesium alloys under the condition of a large ER was analyzed.

## 2 Materials and Methods

AFE is a process method in which two or more split stems replace the traditional overall structure for alternating downward loading, as shown in Fig. 1. According to the difference in the periodic loading mode of each split stem, the alternating extrusion techniques can be divided into progressive and interactive methods. The additional shear deformation provided by the alternate downward loading of the split punch can increase the mechanical properties while weakening the texture of the formed product and can ensure that the product shape and performance are perfectly matched.

The experimental billet is a cylinder with a diameter and height of 40 mm. The specific components are shown in Table 1. The billet had to be homogenized before the experiment. To ensure that the temperature did not fluctuate more than 1 K, a thermocouple was employed to monitor it in real time. The extrusion test was carried out on a

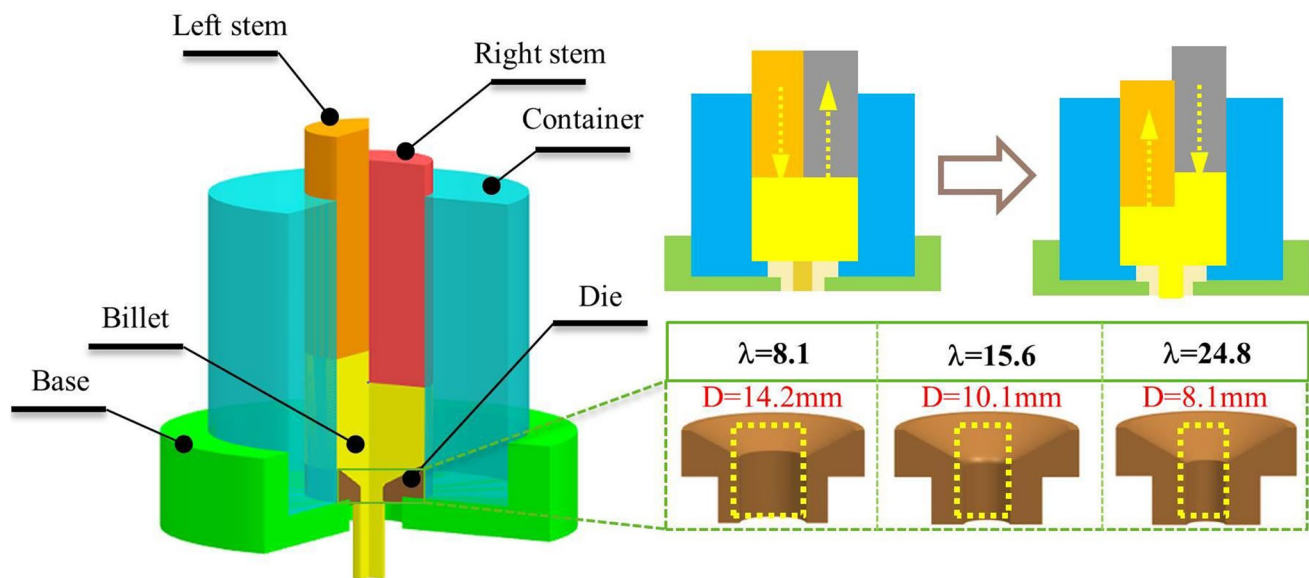


Fig. 1 AFE process principle

**Table 1** Chemical composition of AZ31 magnesium alloy (wt%)

| Al   | Zn   | Mn   | Fe     | Si    | Cu     | Ni      | Mg   |
|------|------|------|--------|-------|--------|---------|------|
| 3.20 | 0.86 | 0.36 | 0.0018 | 0.021 | 0.0022 | 0.00056 | Bal. |

YT32-100 press, with water-based graphite as a lubricant, forming temperature was 623 K, the extrusion speed was 1 mm/s, and ERs were 8.1, 15.6, and 24.8.

The samples of 7 mm × 4 mm × 3 mm were cut out from the center of the sample with different ERs, which were used for metallographic observation and EBSD. The samples were successively ground on #80, #400, #1500, #3000, and #5000 sandpaper, and mechanical polishing was performed until the surface of the sample was bright and free of apparent scratches. The metallographic etching solution is used to treat the sample after being mechanically polished. After the samples had been etched, they were investigated using an optical microscope. To prepare EBSD test samples, the etched samples were mechanically polished again and then electropolished. The electrolytic solution was a mixture of phosphoric acid and alcohol solution (volume ratio was 3:5). After many experiments, the polishing effect was the best when the current was 0.3 A and 0.2 A for 60 s, and the total time was 120 s.

For electron backscatter diffraction studies, a field emission electron microscope was used to examine electrolytically treated materials. To study the hardness of the extruded products under different conditions, the hardness of the samples was determined using a Vickers hardness tester and 10 points were measured at the center of each sample to reduce the test error.

### 3 Results and Discussion

#### 3.1 Microstructure

Figure 2 expresses the band contrast (BC) maps and AZ31 magnesium alloy characteristics of grain morphology under various ERs, and the grain boundary is obvious in all BC images. Figure 2a) shows the metal structure under an ER of 8.1. The grain size is relatively uniform. The maximum grain size is 43.7  $\mu\text{m}$ , and the average grain size is 10.53  $\mu\text{m}$ . Figure 2b) shows the grain structure morphology under an ER

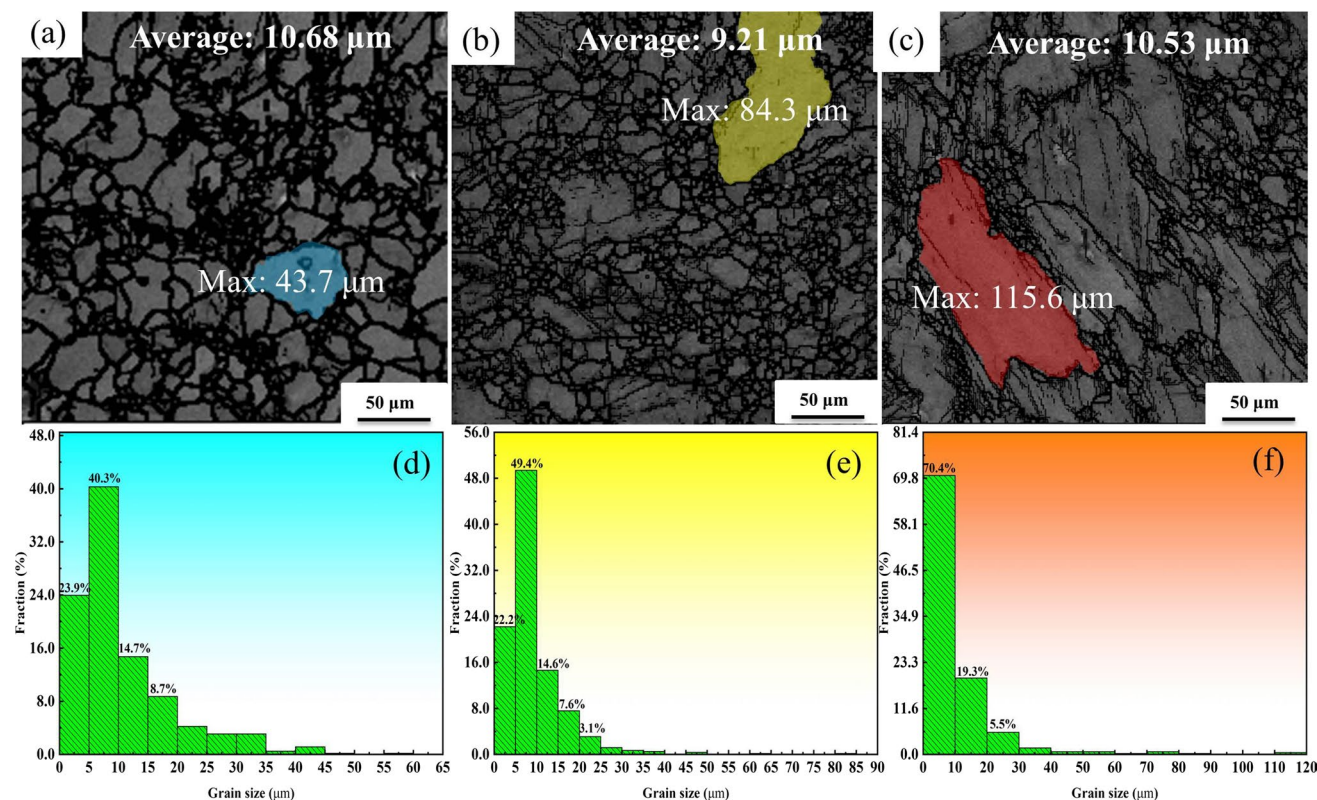


**Fig. 2** At various ERs, grain size distribution and BC images: **a, d**  $\lambda = 8.1$ ; **b, e**  $\lambda = 15.6$  and **c, f**  $\lambda = 24.8$



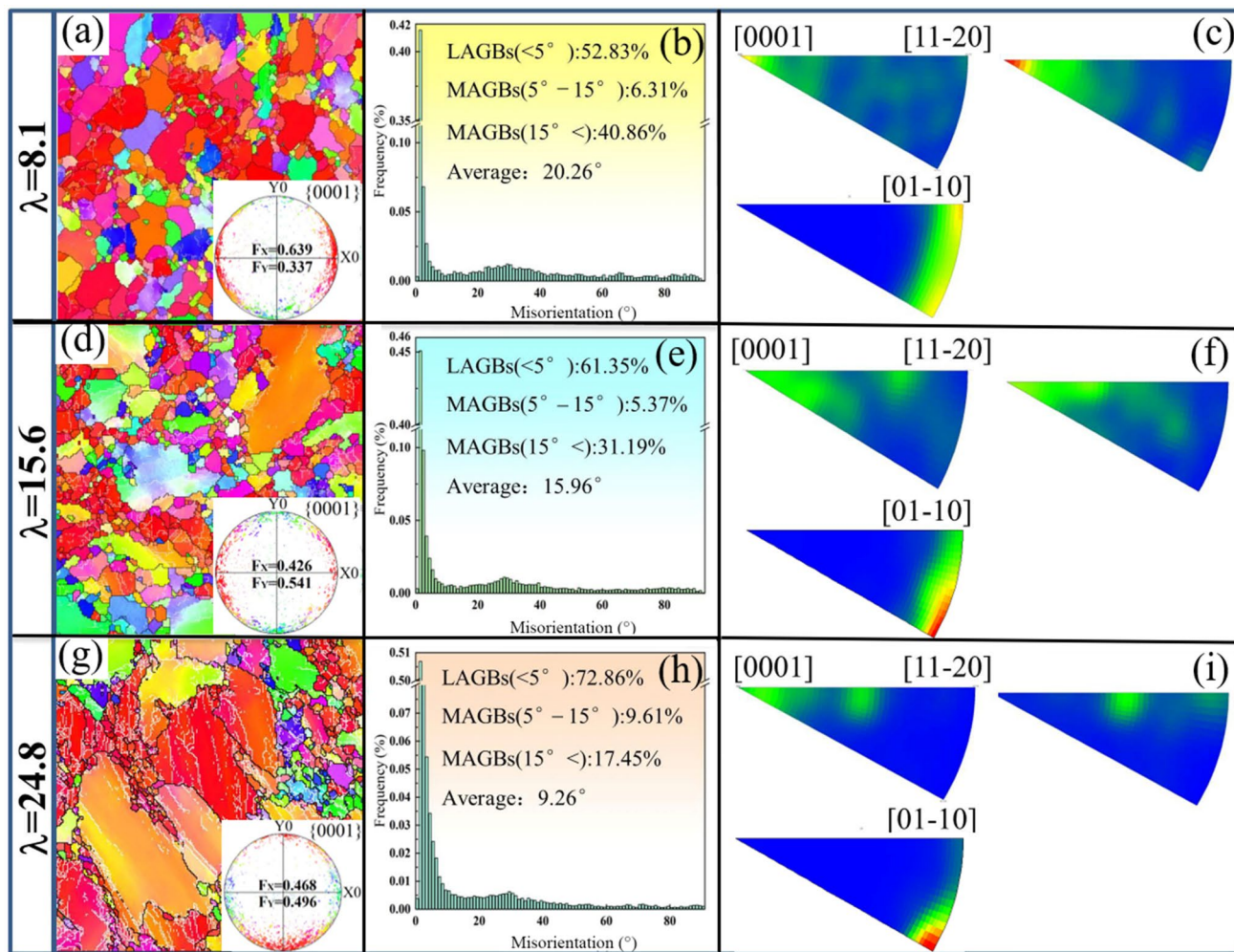


Fig. 3 EBSD maps at different ERs: a, b, c  $\lambda=8.1$ ; d, e, f  $\lambda=15.6$  and g, h, i  $\lambda=24.8$

of 15.6. The grain size difference gradually intensified; the maximum grain size reached 84.3  $\mu\text{m}$ , and the minimum was only 3.32  $\mu\text{m}$ . The grain morphology is illustrated in Fig. 2c) when the ER is 24.8, and the largest grain size even reaches 115.6  $\mu\text{m}$ , as can be observed. The LAGBs (low-angle grain boundaries) are densely distributed in grain. The smallest grain is only 2.28  $\mu\text{m}$ . The average grain size is 11.43  $\mu\text{m}$ . As the ER rises, the grain size disparity at the same location widens substantially.

According to Guan et al. [17], extrusion parameters can have a substantial impact on the Zener–Hollomon ( $Z$ ) parameter, which is the crucial factor affecting grain size. Derby [19] reported in research that a higher  $Z$  value could effectively refine recrystallized grains, satisfying Eq. (1):

$$Zd_{\text{DRX}}^p = \text{constant} \tag{1}$$

where  $d_{\text{DRX}}$ ,  $p$ , and  $Z$  represent the average DRXed grain size, the relevant exponent, and the Zener–Hollomon parameter, respectively. The Zener–Hollomon parameter was computed by Watanabe et al. [20], as shown in Eq. (2):

$$z = \epsilon \exp\left(\frac{Q}{RT}\right) \tag{2}$$

where  $R$ ,  $T$ ,  $Q$ , and  $\epsilon$  represent the gas constant (8.314 J/mol K), the processing temperature, the activation energy (Mg: 135 kJ/mol) for lattice diffusion, and the strain rate. Equation (3) can be used to calculate  $\epsilon$ :

$$\epsilon = \frac{D_B^2 V_R \ln \lambda}{D_B^3 - D_E^3} \tag{3}$$

$V_R$  (the ram speed),  $D_E$  (the diameter of the extrudate),  $D_B$  (the diameter of billet), and  $\lambda$  (the ER). They are bringing the corresponding values into Eqs. (1), (2), and (3), and we find

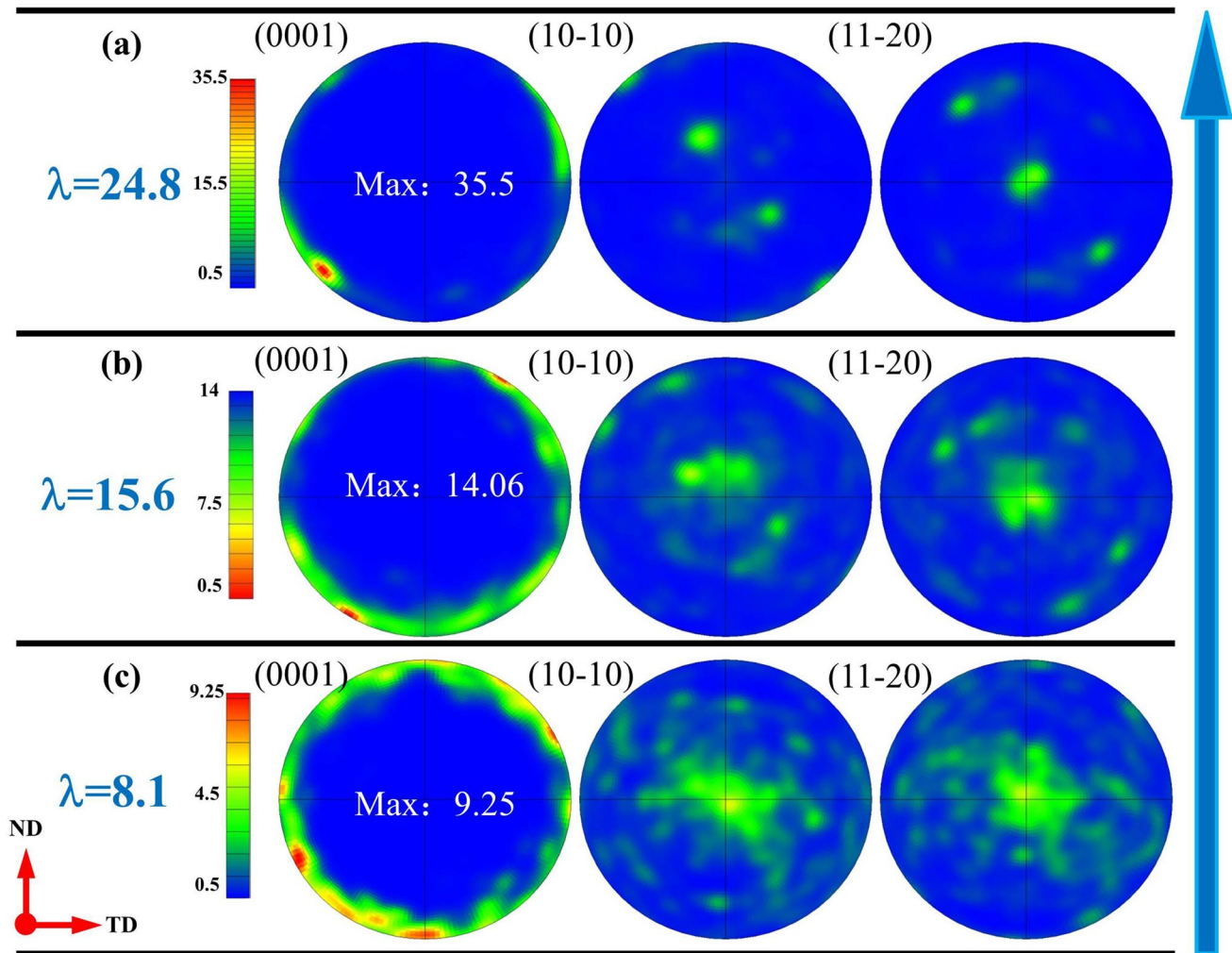


**Fig. 4** Pole figures: **a**  $\lambda = 24.8$ , **b**  $\lambda = 15.6$ , and **c**  $\lambda = 8.1$

that  $Z$  increases with increasing ER. According to Eq. (1), grain size is inversely related to the  $Z$  value. Grains are gradually refined as the ER increases. However, this study is different from conventional extrusion, the internal structure of alternating extrusion does not gradually refine with increasing ER; when the ER is 24.8, the average grain size increases. This rather contradictory result may be due to frictional heat and deformation heat during hot extrusion with a higher ER, frictional heat and deformation heat are not considered in the above calculations [16]. When the ER is large, frictional heat and deformation heat have a significant effect on microstructure evolution. Heat generation caused by friction and deformation is a very common phenomenon in conventional extrusion. According to Liu et al. [21], the evolution of temperature as a combined result of deformational and frictional heating is a more serious concern, and therefore, the phenomenon of grain coarsening at a large ER still needs to be further studied, and the grain refinement mechanism will be analyzed in the following. Ross et al.

[24] indicated the temperature rise caused by heat generated during deformation is crucial in promoting grain growth. In addition, the unique loading mode of AFE will also have a significant impact on grain refinement. In the above metallographic structures, the grain size is generally concentrated in 0–10  $\mu\text{m}$ . The refined grains are distributed around the coarse grains. The local region is a Bimodal-grained structure according to Zheng et al. [23], AFE provides a new idea for extrusion technology to produce multimodal-grained alloy structures.

At various ERs, Fig. 3 displays the distribution of misorientation angles and Inverse Pole Figure maps of the AZ31 magnesium alloy. The [0001] of most grains is parallel to AGB or ND, as illustrated in Fig. 3a. In Fig. 3d, g combined with f, i the grain orientation is mainly concentrated in the direction of [1–10]. As shown in Fig. 3b, e, and h, the misorientation angles of all the alloys have one feature in common. (The histogram shows a single peak). HAGBs can frequently become the nucleation point

of dynamic recrystallization due to grain boundary expansion, according to Li et al. [24]. In addition, as the ER increases gradually, LAGBs drop from 52.83 to 72.86%, high-angle grain boundaries (HAGBs) fall from 40.86 to 17.15%, and the average orientation difference angle also decreases to 9.26.

In polycrystalline magnesium alloys, the deformation behavior and mechanical properties of metal materials are dominated by their lattice structure. The properties of materials are not a simple superposition of the properties of a single grain. The texture can broadly be defined as grain orientation concentrated in or near some direction, according to Chen and Jiang [25]. The directional rotation of grains during plastic deformation will cause deformation texture. Figure 4 shows the comparison of pole figures under different ERs. As the ER increases, the texture gradually sharpens. When the ER is 24.8, the texture intensity even reaches 35.5. The typical fiber texture is destroyed. The degree of deformation can significantly affect the texture intensity, which is further reflected in this paper recrystallization behavior and grain size are also linked to texture intensity [26]. When the ER is the highest (as shown in Fig. 3), the coarse grains are entirely red–orange.

## 4 Mechanical Properties

In most cases, the increased strength of a material compromises its ductility, but grain refinement can improve both the strength and ductility of magnesium alloys. The above results show that when the ER increases from 8.1 to 15.6, the grains are refined after alternate extrusion, but when the ER is 24.8, the average grain size increases instead. The hardness values under different conditions measured under 25 g pressure holding load, 10 s time and 20 °C temperature are shown in Fig. 5 (5 points were measured at the center of each 10  $\mu\text{m}$  to reduce the test error). Generally, the factors affecting hardness include grain size, dislocation density, and second phase particles. However, the second phase particles have a minor influence in the homogenized AZ31 magnesium alloy, so the density of dislocations and the size of grains can have a significant impact on sample hardness. Figure 5 shows that the hardness of the products with the largest ER is lower, and the average hardness is only 54.86 HV. When  $\lambda = 15.6$ , the hardness of the product is the highest (67.79 HV). In contrast to  $\lambda = 24.8$ , the hardness of  $\lambda = 15.6$  increased by 23.7%. The effect of dislocation density on hardness cannot be ignored. In the following, the dislocation density of products with different ERs will be analyzed.

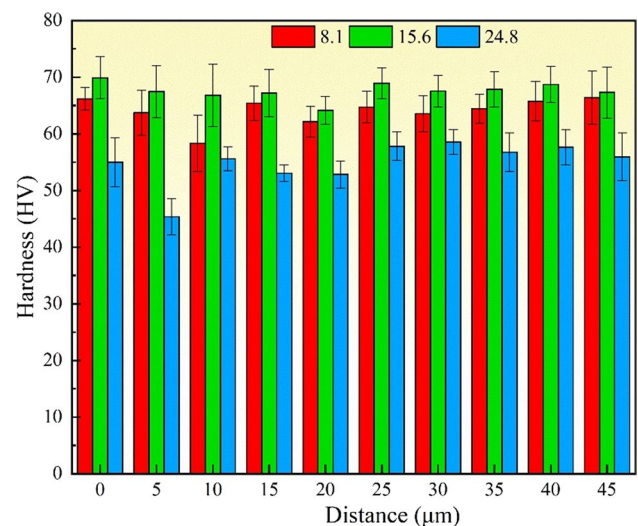
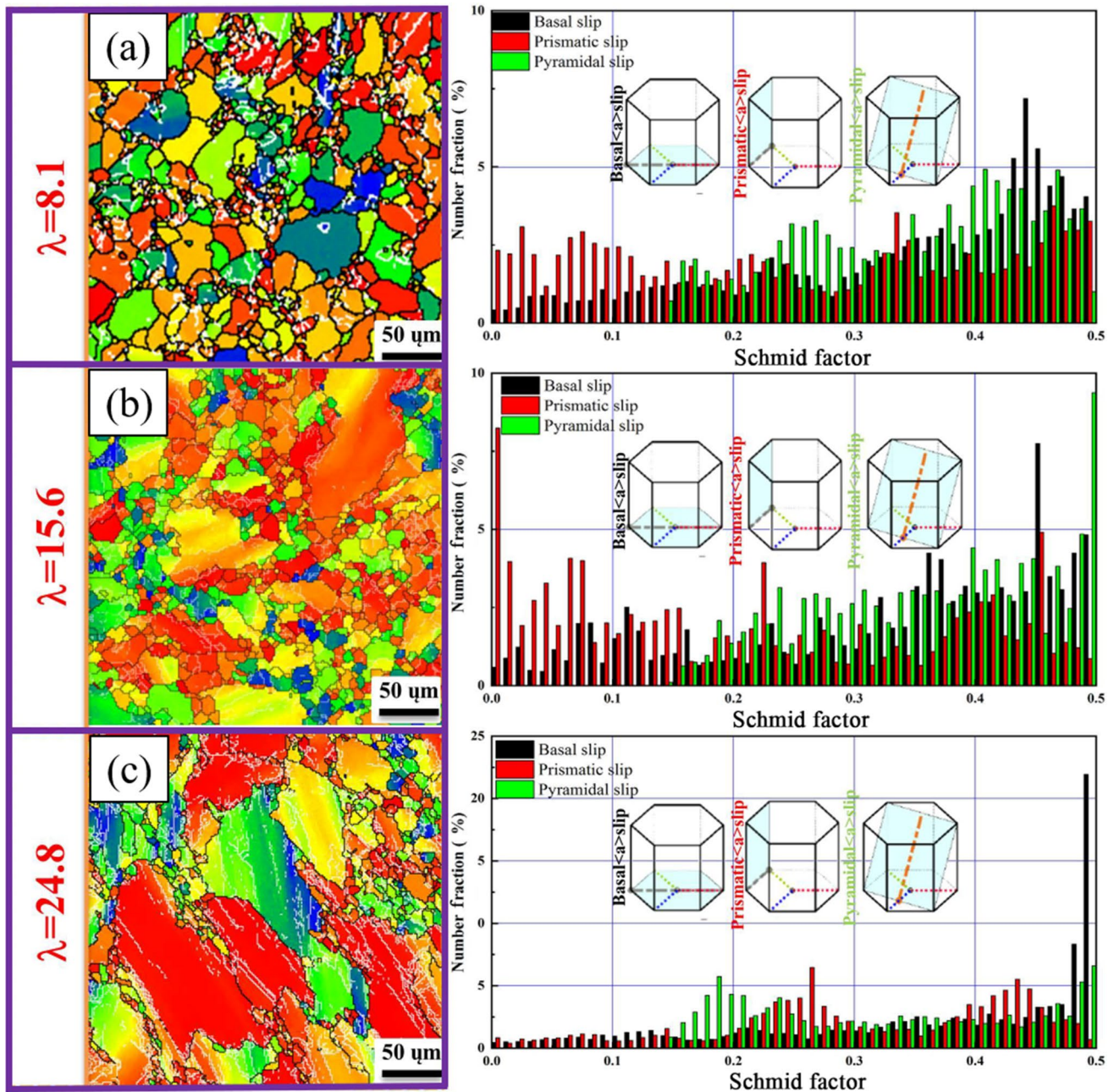


Fig. 5 Hardness of each ER

## 5 Deformation Mechanism

To investigate the mechanism of deformation at different ERs, the Schmid factor data were extracted using channel 5 software. Lou et al. [27] indicated that the stress state of the crystal material satisfies the yield criterion and plastic deformation will occur. Plastic deformation is caused by shear stress, and the slip process can only start when the slip plane of resolved shear stress along the slip direction reaches a specific value. Figure 6 shows the Schmid factor of products at different ERs. The Schmid factor values are shown in the histograms. For hexagonal close-packed metals, Cepeda-Jimenez et al. [28] reported that the (critical resolved shear stress) CRSS ratio of prismatic slip to base slip can be used to measure the degree of difficulty of prismatic slip; the larger the ratio is, the harder the slip. When the ER is 8.1, the average Schmid factor of base slip is 0.36, the average Schmid factor of prismatic slip is 0.31, the average Schmid factor of pyramidal slip is 0.32, and the activation ability of base slip is the largest. When the ER is 15.6, the SF values of the basal plane, prismatic slip, and pyramidal slip are 0.32, 0.21, and 0.35, respectively. Pyramidal slip is activated to a certain extent, while pyramidal slip can reduce the plastic anisotropy of magnesium single crystals according to Sandlobes et al. [29]. When the ER reaches the maximum, the SF value of pyramidal slip reaches the highest value, which is 0.36. The commencement of pyramidal slip is easier with the progressive increase in the ER. According to Nan et al. [30], basal slip and prismatic slip of magnesium alloys provide a restricted number of slip systems that do not fully meet the Von-Mises criteria. The basal slip and prismatic slip must be  $\langle a \rangle$  dislocation slip, and the slip direction is  $\langle 11\text{--}20 \rangle$  parallel to the basal plane. To make the magnesium alloy have good





**Fig. 6** SF values for various slip systems under different ERs: **a**  $\lambda = 8.1$ ; **b**  $\lambda = 15.6$  and **c**  $\lambda = 24.8$

uniform plastic deformation ability, it is necessary to use twinning or fully activate the potential pyramidal slip [31].

## 6 Calculation of Geometrically Necessary Dislocation

To analyze the evolution process of the microstructure deeply under different conditions, the kernel average misorientation (KAM) of the product transverse direction

(TD)–normal direction (ND) plane is shown in Fig. 7. As the ER increases, KAM gradually increased from  $0.837^\circ$  to  $1.24^\circ$ . Figure 7g, h) and I) shows the L1, L2, and L3 misorientation angle distributions of coarse grains at different ERs, respectively. As the ER increases, the strain accumulated inside the grains also increases. For further analysis, the GND [32] in Fig. 7 was calculated. The GND can be calculated by  $\rho \approx \theta/(b\delta)$  (where  $\theta$  is the accumulated misorientation angle in radians within a distance  $\delta$  and  $b$  is the Burgers vector) according to Li et al. [33]. Taking



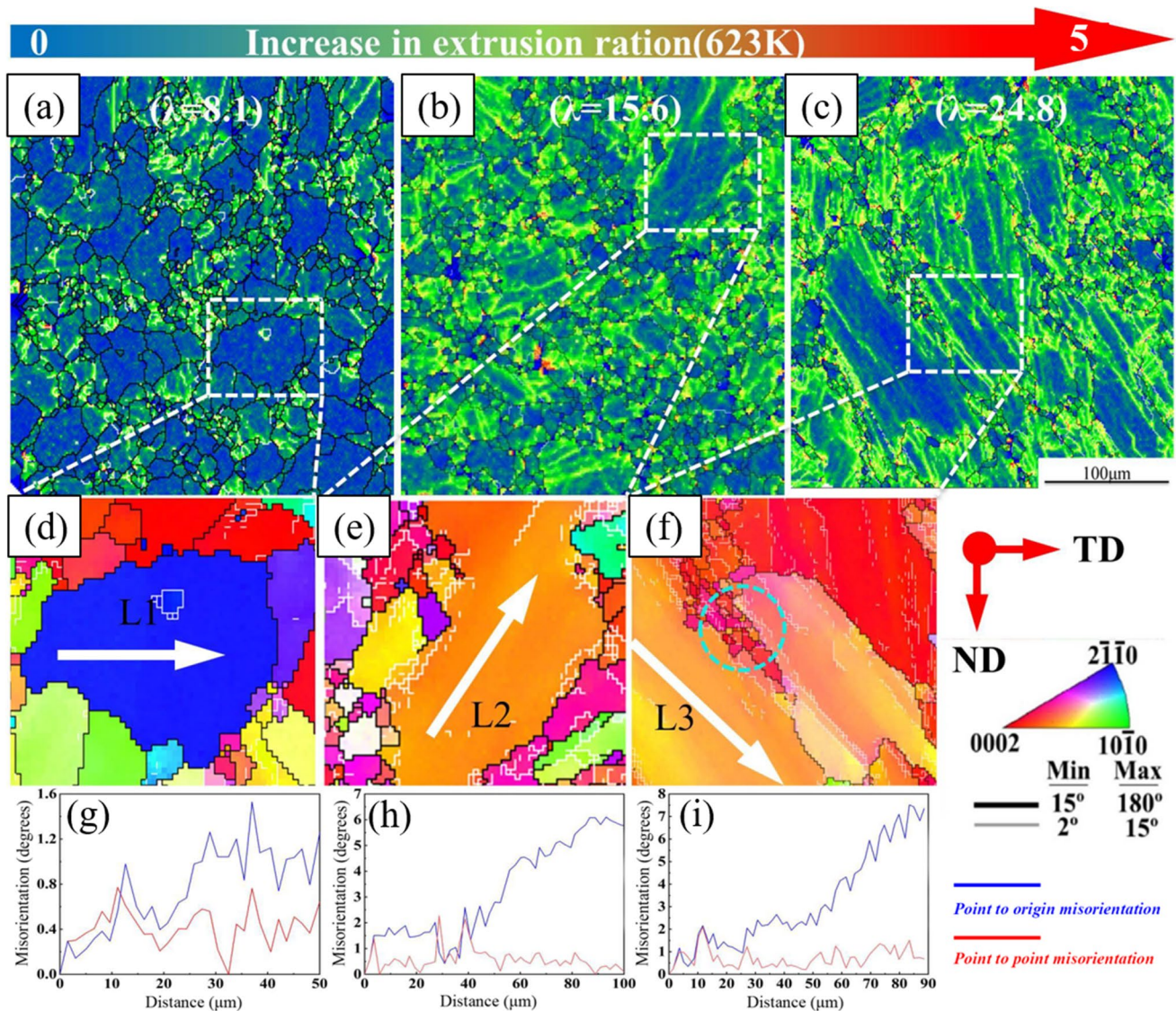


**Fig. 7** Sample in the TD-ND plane after extrusion at 350 °C: **a**  $\lambda = 8.1$ ; **b** and **c** details of  $\lambda = 15.6$  and  $\lambda = 24.8$ , respectively; **d–i** corresponding misorientation profiles measured along lines L1, L2 and L3

$b = 3.2 \times 10^{-10}$  for pure Mg [34]. According to the misorientation distribution in Fig. 7, it can be calculated that under the three ERs, the GNDs are  $5.2 \times 10^{-12}$ – $6.1 \times 10^{-14} \text{ m}^{-2}$  ( $\lambda = 24.8$ ),  $4.2 \times 10^{-13}$ – $1.3 \times 10^{-15} \text{ m}^{-2}$  ( $\lambda = 15.6$ ) and  $1.2 \times 10^{-14}$ – $1.0 \times 10^{-15} \text{ m}^{-2}$  ( $\lambda = 8.1$ ). More dislocations accumulate in the coarse grains with larger extrusions.  $\rho = 2\phi/(\mu b)$  from Chiu et al. [35] can calculate GND also, where  $\mu$  is 1300 nm and  $\phi$  is evaluated from the KAM map corresponding to Fig. 7. According to the KAM map, a certain prediction can be made about the recrystallized fraction of the product, because the recrystallization process can consume a large amount of distortion energy. Therefore, it can be preliminarily judged that the recrystallization ratio is higher at  $\lambda = 8.1$ . In addition, the dislocation density also has a certain degree of influence on the hardness. In the study of Xu

et al. [36], the dislocation density can be consistent with the hardness test results. By contrast, their conclusions are different from the results of this paper, so the grain refinement mechanism is discussed below.

## 7 DRX Behavior

Recrystallization significantly affects the microstructure morphology. Figure 8 shows the distribution of dynamically recrystallized grains, sub-grain structures and deformed grains under various ERs. The recrystallization proportion reaches 33.6%, when the ER is the smallest. When the ER is 15.6, recrystallization proportion takes second place, and recrystallized grains are often generated between coarse



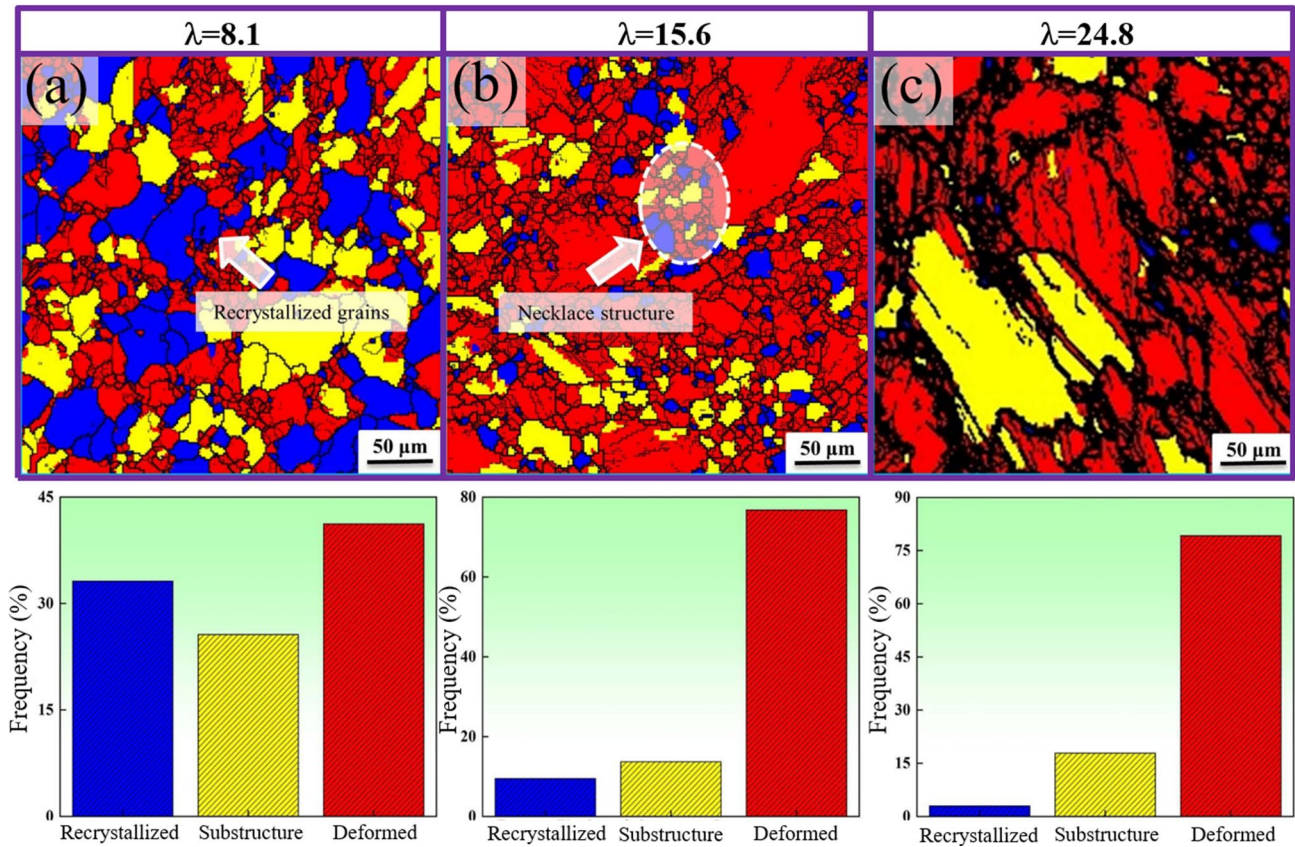


**Fig. 8** Different grain types of grains: **a**  $\lambda=8.1$ ; **b**  $\lambda=15.6$ ; **c**  $\lambda=24.8$

grain boundaries to form a necklace structure, as shown in Fig. 8b, which is one of the signs of discontinuous dynamic recrystallization (DDRX) according to Fatemi-Varzaneh et al. [37]. When the ER is 24.8, the proportion of recrystallization is 2.92%. As the ER rises, the proportion of recrystallized grains decreases, which corresponds to the estimated dislocation density in Fig. 7. Recrystallization is essentially a process in which new grains without distortion are produced in the deformed structure, and the dislocation density is significantly reduced.

To explore the cause of tissue coarsening of grains and high texture intensity under the maximum ER, samples with an ER of 24.8 were analyzed. Figure 9 shows EBSD maps when  $\lambda=24.8$ . There are many fine recrystallized grains distributed among the coarse deformed grains in Fig. 9. Figure 9b) shows that MAGBs (medium angle grain boundaries, grain boundary misorientation angle  $5^\circ < \theta_{GB} < 15^\circ$ ) and LAGBs are densely distributed at  $\lambda=24.8$ . MAGBs can be regarded as the intermediate stage from LAGBs to HAGBs. (MAGBs are marked in red, and LAGBs are marked in green). Combined with the analysis of Fig. 3, the proportion of LAGBs is the largest when  $\lambda=24.8$ , LAGBs are concentrated at the junction of coarse grains, and some regions are accompanied by the rotation of sub-grain boundaries.

LAGBs and MAGBs can be seen in new DRXed grains, which indicates that the LAGBs are changing to a high-angle sub-grain boundary. Jiang et al. [38] showed that this microstructure evolution accompanied by the continuous rotation of sub-grains is characteristic of continuous dynamic recrystallization (CDRX). In Fig. 9c, d, we can better comprehend the reasons for texture evolution in Fig. 4 by using blue to represent un-recrystallized grains and gray to represent recrystallized grains. The texture of  $\lambda=24.8$  is mainly composed of unDRXed grains. (1) [0001] fiber orientations, such as grain G1, and (2) non-basal orientations, such as grains G2 and G3 (the  $c$ -axis is approximately  $43.35^\circ$  between [0001] and [10]). At the same time, many fine grains are mixed between grains G2 and G3 and extend inward along the grain boundary.

The typical un-recrystallized grain G2 in Fig. 9 is analyzed separately to explore the recrystallization mechanism of  $\lambda=24.8$  (Fig. 10). Figure 10 clearly shows that the grains are divided into orange and yellow, which indicates two different grain orientations. According to Fig. 10b, c, the grain of orientation is between [0001] and [10]; however, there is still a  $6^\circ$ – $8^\circ$  misorientation between the yellow area and the orange area, which can be further confirmed by the hexagonal prism inserted along AB in Fig. 10a. The misorientation

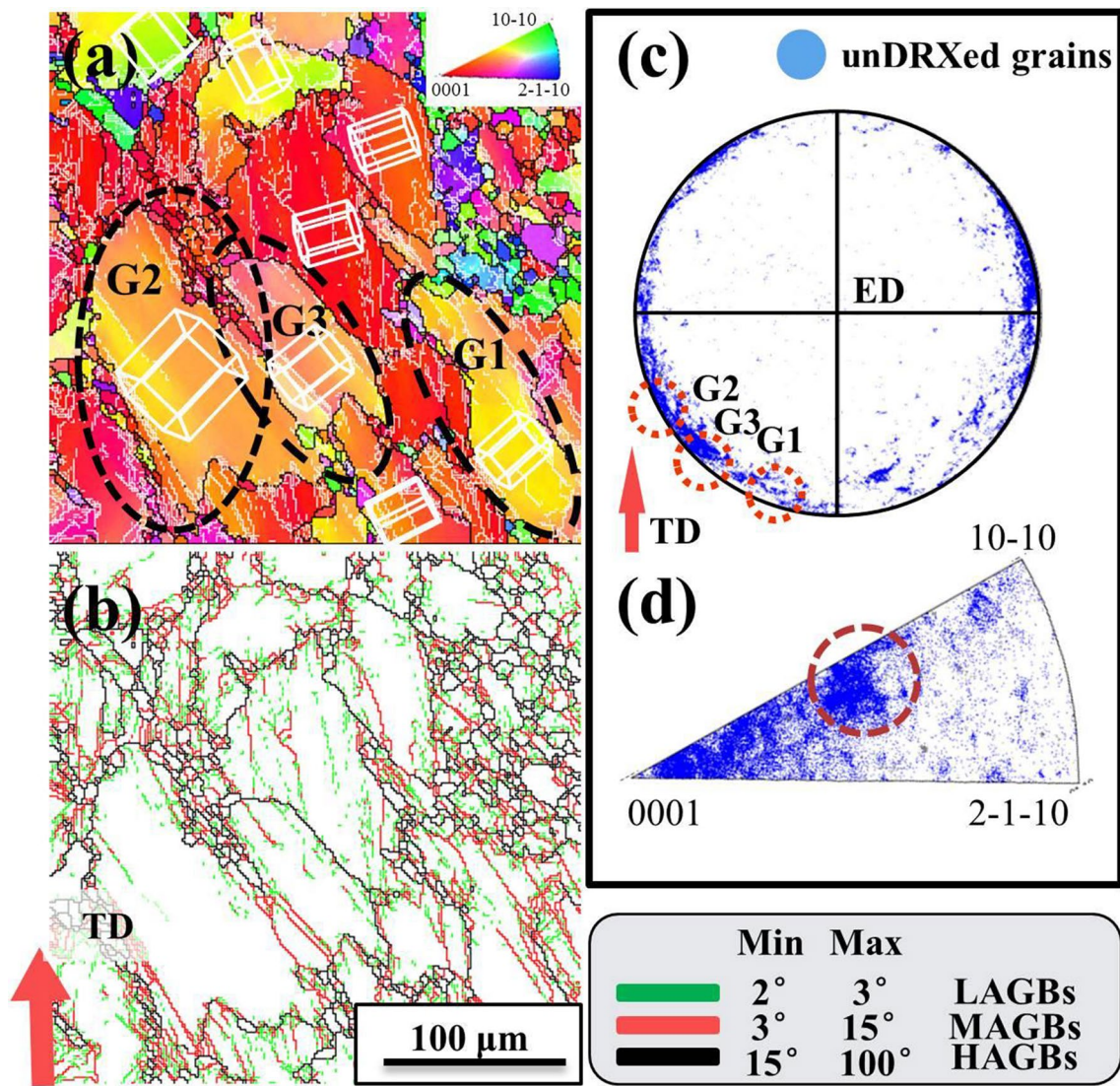
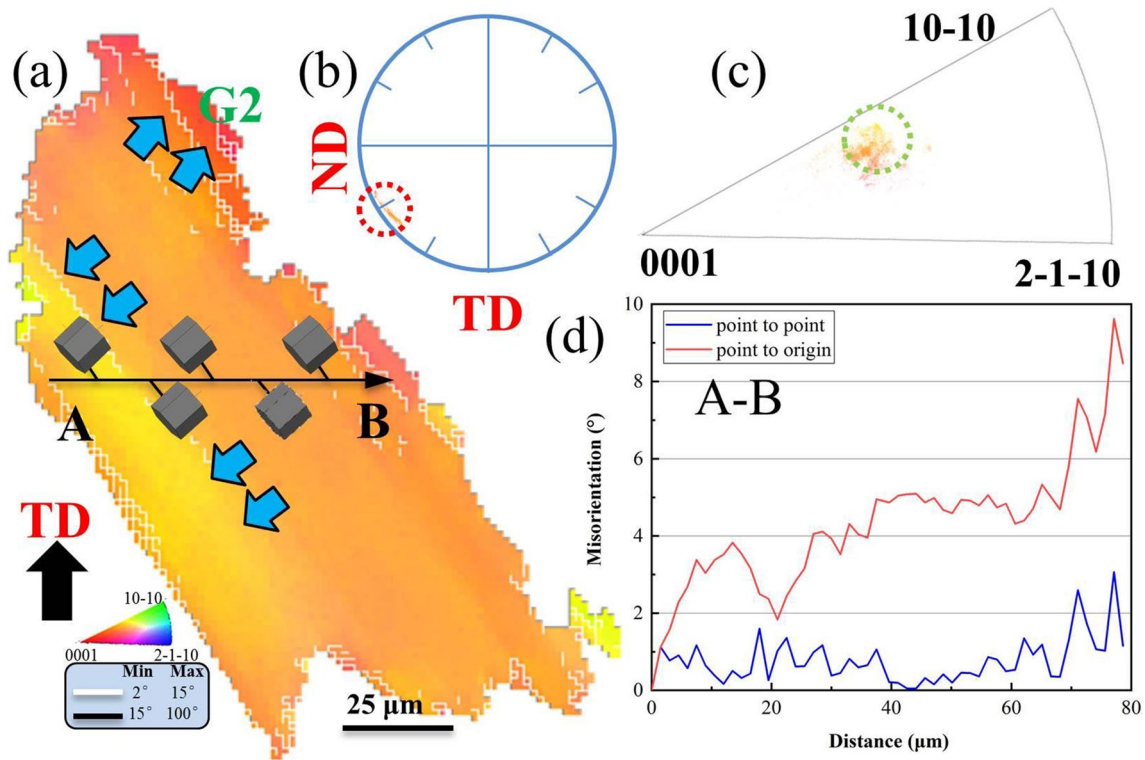


Fig. 9 EBSD results of  $\lambda = 24.8$ : **a** IPF map, **b** corresponding boundary misorientation map and **c** (0001) pole figure, and **d** inverse pole figure

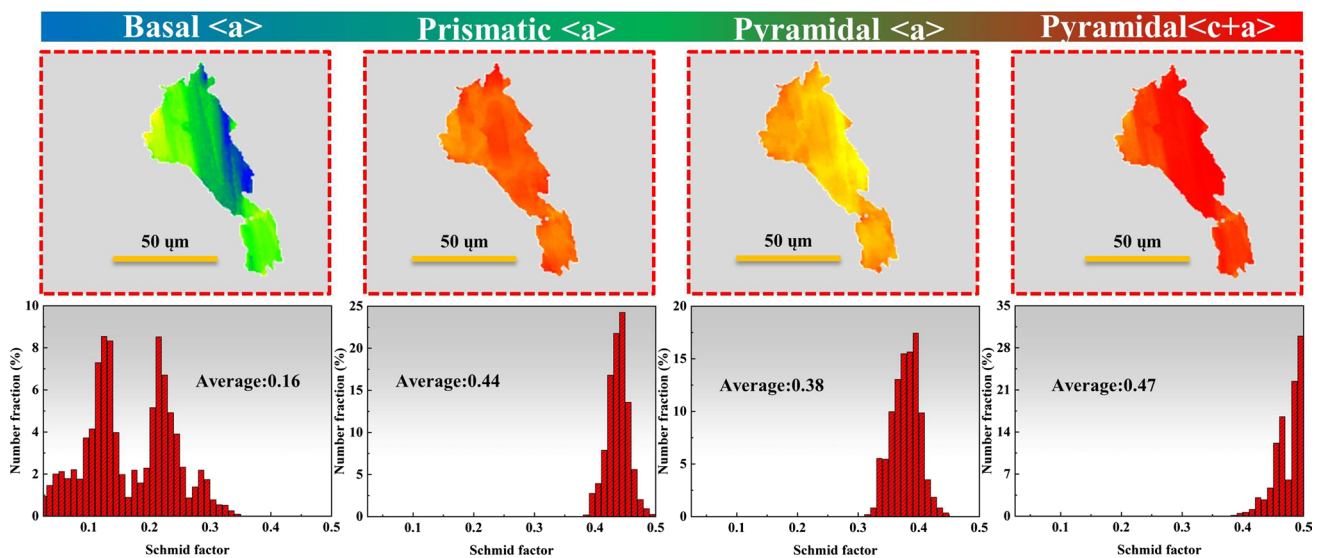
analysis is carried out along the contour line AB of the black arrow, and the variation in the misorientation angle in the range of 80 μm is given in Fig. 10d. The cumulative misorientation angle reaches 10° with increasing distance, the misorientation angle point to point is between 0° and 3°, and the grain misorientation changes continuously. Usually, Gui et al. [39] showed that LAGBs are caused by the formation of substructures in accumulated dislocations or deformed structures. The CDRX mechanism allows these LAGBs to capture more moving dislocations and turn themselves into HAGBs, which then transform the sub-grains into new DRXed grains. According to Sakai et al. [40], therefore, the coarse grains will be recrystallized by CDRX under further deformation.

Figure 11 shows various slip systems of a single coarse grain and their corresponding histograms at an ER of 24.8. There are two colors of blue and green at the same grain. For basal  $a >$  slip, the average SF was 0.16, which is the smallest among the four slip systems, indicating the high mobility of non-basal slip dislocations according to Srinivasarao et al. [41]. Continuous dynamic recrystallization occurs by non-basal  $\langle a \rangle$  cross slip. Thus, the large amount of LAGBs in the grain can be attributed to dislocation rearrangement caused by cross-slip and climbing. As the deformation process progresses, LAGBs merge and rotate through the continuous absorption of dislocation energy, which transforms into high-angle grain boundaries and recrystallized grains, which is typical of CDRX.





**Fig. 10** UnDRXed grain G2: **a** inverse pole figure, **b** (0001) pole figure, **c** inverse pole figure and **d** line profile of misorientation angle along the arrows AB



**Fig. 11** SF of unDRXed grain as shown in Fig. 9a

In summary, by analyzing the EBSD maps when the ER is 24.8, CDRX is the predominant recrystallization method in the products with the highest ER, according to preliminary findings. This is a process in which deformed grains

are broken and refined; Dynamic recrystallization is not yet complete in broken and refined grains. Grain boundary rotation and dislocation climbing did not promote the annihilation of high-density dislocations at grain boundaries, thereby

relaxing the grains to form recrystallized grains, which led to the identification of deformed grains in the EBSD test. Therefore, when the ER is 24.8, the grains are relatively coarse, and CDRX will lead to texture sharpening, which is not conducive to weakening the anisotropy of the magnesium alloy.

## 8 Conclusions

1. The results of the comparative study on the grain size and hardness of the AFE under different conditions show that the average grain size was refined to 7.13  $\mu\text{m}$  when the ER increased from 8.1 to 15.6. The hardness of the extruded product was 67.8 HV. However, when  $\lambda$  continued to rise to 24.8, the grain size increased. The hardness value decreased significantly by 23.5% compared with the condition of  $\lambda = 15.6$ .
2. Compared with other conditions, the average grain size of the  $\lambda = 15.6$  is the smallest, which is only 7.13  $\mu\text{m}$ , and the dislocation density is larger. Grain refinement promotes the improvement of metal material properties. At the same time, the greater the dislocation density of the product is, the higher the strength ( $S$ ) of the metal material. The synergistic effect of grain refinement and dislocation density change improves the hardness. Therefore, the hardness of the product is the highest when  $\lambda = 15.6$ .
3. CDRX is the main grain refinement mechanism at  $\lambda = 24.8$ . LAGBs account for the largest proportion and are mainly concentrated at the junctions of coarse grains, and some regions are accompanied by the rotation of sub-grain boundaries. As the deformation process progresses, non-basal slip  $\langle a \rangle$  dislocations are activated and enriched near LAGBs, and these dislocations are continuously absorbed by LAGBs to form CDRX.

**Acknowledgements** This project is supported by the National Natural Science Foundation of China (No. 51975166) and the Natural Science Foundation of Heilongjiang Province (No. JQ2022E004).

## Declarations

**Conflict of interest** This manuscript has not been published or presented elsewhere in part or in entirety and is not under consideration by another journal. We have read and understood your journal's policies, and we believe that neither the manuscript nor the study violates any of these. There are no conflicts of interest to declare.

## References

- [1] Y. Wang, F. Li, Y. Wang, X.M. Xiao, J. Magnes. Alloy. (2021). <https://doi.org/10.1016/j.jma.2021.05.007>
- [2] P.D. Huo, F. Li, Y. Wang, X.M. Xiao, Int. J. Adv. Manuf. Technol. **118**, 55 (2022)
- [3] H.B. Dai, L. Wang, B.L. Dong, J. Miao, S.B. Lin, H.T. Chen, Mater. Lett. **64**, 27 (2022)
- [4] Y. Yang, X.M. Xiong, J. Chen, X.D. Peng, D.L. Chen, F.S. Pan, J. Magnes. Alloy. **9**, 705 (2021)
- [5] P.D. Huo, F. Li, R.Z. Wu, R.H. Gao, A.X. Zhang, Mater. Des. **219**, 110696 (2022)
- [6] W. Yang, G.F. Quan, B. Ji, Y.F. Wan, H. Zhou, J. Zheng, D.D. Yin, J. Magnes. Alloy. **10**, 195 (2022)
- [7] Y.Q. Chai, C.J. Boehlert, Y.F. Wan, G.H. Huang, H. Zhou, J. Zheng, Q.D. Wang, D.D. Yin, Metall. Mater. Trans. A **52**, 449 (2021)
- [8] X. Li, T. Al-Samman, S. Mu, G. Gottstein, Mater. Sci. Eng. A **528**, 7915 (2011)
- [9] Q.H. Wang, B. Jiang, A. Tang, S.X. Ma, Z.T. Jiang, Y.F. Chai, B. Liu, F.S. Pan, Mater. Sci. Eng. A **689**, 395 (2017)
- [10] Y. Wang, F. Li, N. Bian, H.Q. Du, P.D. Huo, J. Magnes. Alloy. (2021). <https://doi.org/10.1016/j.jma.2021.08.035>
- [11] D. Sagapuram, M. Efe, W. Moscoso, S. Chandrasekar, K.P. Trumble, Acta Mater. **61**, 6843 (2013)
- [12] J. Xu, B. Jiang, J.F. Song, J.J. He, P. Gao, W.J. Liu, T.H. Yang, G.S. Huang, F.S. Pan, Mater. Sci. Eng. A **732**, 1 (2018)
- [13] L.W. Lu, C.M. Liu, J. Zhao, W.B. Zeng, Z.C. Wang, J. Alloy. Compd. **628**, 130 (2015)
- [14] F. Li, X. Zeng, Q. Chen, G.J. Cao, Mater. Des. **85**, 389 (2015)
- [15] O. Ayer, Mater. Sci. Eng. A **793**, 139887 (2020)
- [16] K.K. Alaneme, E.A. Okotete, J. Magnes. Alloy. **5**, 460 (2017)
- [17] K. Guan, R. Ma, J.H. Zhang, R.Z. Wu, Q. Yang, J. Meng, J. Magnes. Alloy. **9**, 1098 (2021)
- [18] X.Z. Jin, W.C. Xu, Z.Z. Yang, C. Yuan, D.B. Shan, B.G. Teng, B.C. Jin, J. Mater. Sci. Technol. **45**, 133 (2020)
- [19] B. Derby, Acta Mater. **39**, 955 (1991)
- [20] H. Watanabe, H. Tsutsui, T. Mukai, K. Ishikawa, Y. Okanda, M. Kohzu, K. Higashi, Mater. Trans. **42**, 1200 (2001)
- [21] G. Liu, J. Zhou, J. Duszczyc, J. Mater. Process. Technol. **186**, 191 (2007)
- [22] N.G. Ross, M.R. Barnett, A.G. Beer, Mater. Sci. Eng. A **619**, 238 (2014)
- [23] R.X. Zheng, G.D. Li, Z. Zhang, Y.T. Zhang, S.Y. Yue, X. Chen, K. Ameyama, C.L. Ma, Mater. Res. Lett. **7217**, 224 (2019)
- [24] X.Q. Li, L. Ren, Q.C. Le, L. Bao, P.P. Jin, P. Wang, C.L. Cheng, X. Zhou, C.L. Hu, J. Magnes. Alloy. **9**, 937 (2021)
- [25] S. Chen, X. Jiang, Mater. Sci. Eng. A **612**, 267 (2014)
- [26] D.D. Yin, C.J. Boehlert, L.J. Long, G.H. Huang, H. Zhou, J. Zheng, Q.D. Wang, Int. J. Plast. **136**, 102878 (2021)
- [27] X.Y. Lou, M. Li, R.K. Boger, S.R. Agnew, R.H. Wagoner, Int. J. Plast. **23**, 44 (2007)
- [28] C.M. Cepeda-Jimenez, J.M. Molina-Aldareguia, M.T. Perez-Prado, Acta Mater. **84**, 443 (2015)
- [29] S. Sandlobes, M. Friak, S. Zaeffferer, A. Dick, S. Yi, D. Letzig, Z. Pei, L.F. Zhu, J. Neugebauer, D. Raabe, Acta Mater. **60**, 3011 (2012)
- [30] X.L. Nan, H.Y. Wang, Z.Q. Wu, E.S. Xue, L. Zhang, Q.C. Jiang, Scr. Mater. **68**, 530 (2013)
- [31] H. Miyano, K. Takemoto, M. Tsushida, H. Kitahara, S. Ando, Mater. Trans. **62**, 1097 (2021)
- [32] R. Ni, Z.W. Jiang, D.D. Yin, W. Yang, H. Zhou, J. Zheng, Q.D. Wang, Metall. Mater. Trans. A **53**, 535 (2022)
- [33] Y.K. Li, M. Zha, J. Rong, H.L. Jia, Z.Z. Jin, H.M. Zhang, P.K. Ma, H. Xu, T.T. Feng, H.Y. Wang, J. Mater. Sci. Technol. **88**, 215 (2021)
- [34] L.P. Kubin, A. Mortensen, Scr. Mater. **48**, 119 (2003)
- [35] C. Chiu, S.J. Huang, T.Y. Chou, E. Rabkin, J. Alloy. Compd. **743**, 437 (2018)



- [36] M. Wang, X.Y. Xu, H.Y. Wang, L.H. He, M.X. Huang, *Acta Mater.* **201**, 102 (2020)
- [37] S.M. Fatemi-Varzaneh, A. Zarei-Hanzaki, H. Beladi, *Mater. Sci. Eng. A* **456**, 52 (2007)
- [38] M.G. Jiang, C. Xu, H. Yan, G.H. Fan, T. Nakata, C.S. Lao, R.S. Chen, S. Kamado, E.H. Han, B.H. Lu, *Acta Mater.* **157**, 53 (2018)
- [39] Y.W. Gui, L.X. Ouyang, Y.J. Cui, H.K. Bian, Q.A. Li, A. Chiba, *J. Magnes. Alloy.* **9**, 456 (2021)
- [40] T. Sakai, A. Belyakov, R. Kaibyshev, H. Miura, J.J. Jonas, *Prog. Mater. Sci.* **60**, 130 (2014)
- [41] B. Srinivasarao, N.V. Dudamell, M.T. Perez-Prado, *Mater. Charact.* **75101**, 107 (2013)

Springer Nature or its licensor (e.g. a society or other partner) holds exclusive rights to this article under a publishing agreement with the author(s) or other rightsholder(s); author self-archiving of the accepted manuscript version of this article is solely governed by the terms of such publishing agreement and applicable law.